Appendix

A.1 Materials.

The pre-gel alginate solution was prepared by dissolving 2% by weight (w/w) sodium alginate (Sigma Aldrich) in freshly collected deionized (DI) water, to which, 0.01% weight (w/w) of methylene blue dye (Sigma Aldrich) was added to aid visualization. The aqueous calcium bath was prepared by dissolving 150mM of calcium chloride salt in DI water (i.e, 17g of $CaCl_2$ hexahydrate, Sigma Aldrich, in 1000g water), which were filled in clear plastic containers (10cm x 10cm x 12.5cm height). The dynamic viscosity μ of calcium bath was 0.001 Pa.s. Direct measurement of densities (ρ) gave 1054 kg/m^3 for 2% sodium alginate and 1051 kg/m^3 for 150mM calcium chloride solution, and these concentrations of solutions were specifically chosen such that sodium alginate was marginally denser than the calcium bath. The 2% sodium alginate solution was filled in plastic syringes, delivered via a syringe pump and dispensed inside the calcium bath via blunt-tip needles (32G to 12G, inner diametes, $d \sim 0.09 - 1.9$mm respectively). The extrusion flow rates Q_o of the alginate solution was varied between 0.1 ml/min to 20 ml/min. We used new needles for each experiment as it was crucial to maintain a clean unclogged tip. Between each experiment, the calcium bath was stirred to maintain homogeneous ion concentration. The calcium bath was replaced by fresh solution after approximately ten experiments. The radius of the gelled tubes are linearly proportional to the needle radii and weakly depend on the inlet extrusion rate (Fig. A2). For the multiphase composite tubes, embedding fluids such as silicone oil (density, $\rho_{oil} = 972$kg/m^3, kinematic viscosity, 100 cSt) with red dye (silcPig) and compressed nitrogen gas were injected at a flow rate of Q_i (Fig. 5A). By controlling relative rates of Q_o and Q_i, various properties (buoyancy, curvature, stiffness) of the resulting composite fluid-in-solid filaments were controlled. All the experiments were performed at room temperature of 23^o C. For thicker needles (15G-12G, inner diameters, $d \sim 1.4 - 1.9$mm respectively) a 25L plastic tank (41cm x 28cm x 30cm height) was used for the experimental measurements of the coiling instability.

A.2 Experimental Methods

A.2.1 Elastic moduli of the polymerized composite tubes.

The elastic modulus of the extruded polymerized tubes and filaments were measured by bending experiments of the filaments. Small segments ($\sim$ 1-2 cm) of the polymerized filaments were mounted such that its one edge was on a horizontal substrate. The other end was suspended such that gravity could weigh it down. The downward displacement (δ) as a function of the overhung length of the filament from the edge (λ) were measured (Appendix, Fig. A3). A simple calculation using Euler-Bernoulli beam theory gives the solution for the bending profile of the elastic filament due to a distributed load q (force per unit length). In particular, we get

$$\delta = \frac{q\,\lambda^4}{8EI}, \quad I = \frac{\pi\,r^4}{4}, \quad q \equiv \pi r^2\,\rho\,g \implies \lambda^4 = \frac{2Er^2}{\rho g}\delta. \qquad \text{(A.1)}$$

Using the slope of the plot of λ^4 vs δ for freshly crosslinked alginate tubes extracted from solution close to the needle tip (seconds after it has formed, Appendix, Fig.A3 A) and away from the needle tip (several minutes after it has formed, Appendix, Fig. A3 B), the elastic modulus of the filament E can be calculated from the slope of the linear regime $\frac{2Er^2}{\rho g}$ (Appendix, Figs. A3 A-B). Similarly, this experimental setup was used to compare elastic moduli and effective stiffness of fluid-in-solid composite tubes (Appendix, Fig. A3 C). The elastic moduli of the composite tubes were estimated in stretching mode as well, where a filament segment was bent in a 'U' shape and vertically hung from a rigid boundary, and equal weights (metal pins) were placed in the neck of the 'U'. The elastic moduli were then estimated from the slope of the stress (σ)-strain (ε) curves generated from the stretching experiments of the filaments (Figs.5C-D, Appendix, Figs. A3 C-D).

A.2.2 Density of the polymerized composite filaments

For the composite tubes, with inclusions of oil, the effective density of the gelled tubes were estimated as follows. The diameter of the inclusions (n mm) as well as the centre to centre spacing between the inclusions (m mm) were measured from the images (see Fig. 5C). The effective density was then computed as $\rho_{eff} = \frac{n}{m}\,\rho_{oil} + \frac{m-n}{m}\,\rho_{alg}$, where $\rho_{oil} = 972$ kg/m^3 and $\rho_{alg} = 1054$ kg/m^3. The size of the inclusions were varied by selecting a needle diameter for the alginate (15G, $d=$ 1.4mm), then another for the oil (18G, $d=$ 0.84mm), which were connected via a T-junction, and varying the relative flow rates ($Q_o - Q_i$), where Q_o is the outer alginate flow rate and Q_i is the inner oil flow rate (see Fig. 5A).

A.2.3 Curvature measurement from sections of filaments

The curvature of the filaments could be controlled in the following two ways: i) by increasing the extrusion flow rate Q_o, and ii) by placing fluid inclusions at controlled spacing from the central axes of the tubes. For the first case, the polymerized tubes went from smooth to rough as the flow rate Q_o increased, while $Q_i = 0$. The curvature in these cases were quantified as shown in Fig. A4. First, threads were held straight from both ends and placed in calcium chloride solution, after which it relaxed into its preferred shape (see Fig. A4B). Then using the ImageJ software, the image is binarized to extract the desired curve, from which the (x, y) coordinates are extracted and calibrated. Finally a moving least square method[26,27] is used to find a smooth fit of the surface. Once we have a smooth approximation of the curve, we can calculate the curvature of the curve and the corresponding curvature histogram as shown in Figs. A4C-E. In the second case, nitrogen compressed gas was injected at the source of the extruded polymer tube. If the gas bubble were aligned with the central axis of the gelled tubes, the resulting air-filled tubes were straight. However, as they shifted away from the central axis, the tubes became curved, as quantified in Fig. 5B.

A.3 Simulations

To understand the nonlinear dynamics of the coiling filament, we use a discretized model that involves a set of vertices with positions $\mathbf{r}_i$ ($0 \le i \le N+1$) and edges $\mathbf{e}_i \equiv \mathbf{r}_{i+1} - \mathbf{r}_i$ (Fig. A5 A), and

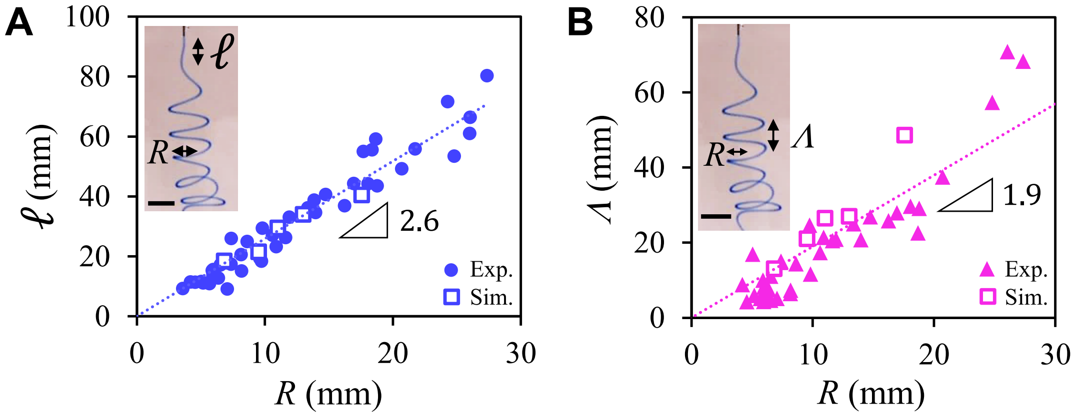

Fig. A1 Characterization of buckling length and vertical spacing in the drag-induced coiling instability. (A) The directly measured buckling length ℓ is plotted as a function of the coiling radius R across various experiments, where needle diameters d varied from 0.1 mm to 2 mm, and flow rates varied from 0.2 ml/min to 20 ml/min. ℓ shows an expected linear correlation with R with a slope of 2.6. Simulations agree well with the experimental data. (Inset) Experimental snapshot to define ℓ and R. (B) Measurement of vertical spacing between adjacent coils Λ of a crosslinked tube during the descent of the coiled helices in the calcium bath during the drag induced instability, as a function of R for both experiments and simulations. (Inset) Experimental snapshot to define Λ and R. Scale bar in both insets is 5 mm.

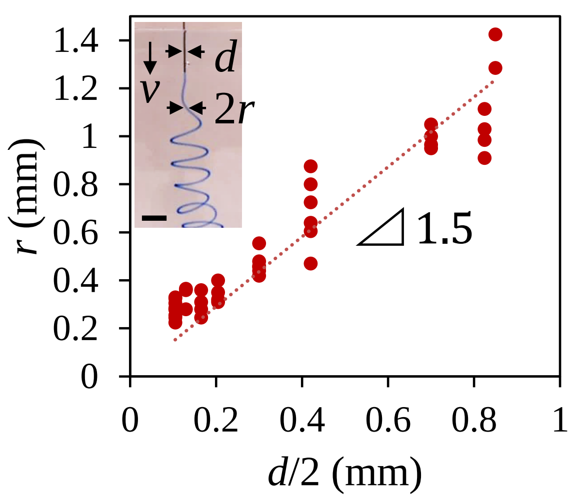

Fig. A2 Experimental characterization of filament radius r as a function of needle inner radius $d/2$. The vertical spread at each value of $d/2$ is due to extrusion velocity v, varying between 1-15 ml/min. Scale bar is 5mm.

assume that the discrete filament is inextensible, and that twisting modes equilibrate rapidly relative to bending modes, so that we can effectively ignore them. The bending energy of this discretized model, localized at the vertices, is associated with the change in angle between two neighboring edges meeting at that vertex, so that the total energy is[28] $\mathscr{E}_b = \frac{1}{2}\sum_{i=1}^{N} \frac{B}{\Delta l_i}\left[2\tan\left(\frac{\theta_i}{2}\right)\right]^2$ where $l_i \equiv |\mathbf{e}_i|$, $\hat{\mathbf{t}}_i \equiv \mathbf{e}_i/l_i$, $\Delta l_i \equiv (l_i + l_{i-1})/2$ and $\cos\theta_i = \hat{\mathbf{t}}_i \cdot \hat{\mathbf{t}}_{i-1}$. Then, the force on the ith vertex is given by

$$\mathbf{F}_i^b \equiv -d\mathscr{E}_b/d\mathbf{r}_i. \tag{A.2}$$

Since the slender filament moves in a viscous liquid at low Reynolds number when inertia is dominated by viscous forces, we use slender-body theory to calculate the drag force[17] which reads

$$\frac{\mathbf{F}_i^{drag}}{\Delta l_i} = -\frac{2\pi\mu}{\log(L/r)}\left[2\mathbf{I}_3 - \hat{\mathbf{t}}_i^T\hat{\mathbf{t}}_i\right]\left(\mathbf{V}_i + \frac{\mathbf{J}_i}{\log(L/r)}\right) - \frac{\pi\mu}{\log(L/r)^2}\left(2\mathbf{V}_i^{\perp} - \mathbf{V}_i^{\parallel}\right), \tag{A.3}$$

$$\mathbf{J}_i = \mathbf{V}_i\log(\Delta l_i) + \sum_{j\neq i}\frac{\Delta l_j}{2|\mathbf{r}_i - \mathbf{r}_j|}\left[\mathbf{I}_3 + \frac{(\mathbf{r}_i-\mathbf{r}_j)^T(\mathbf{r}_i-\mathbf{r}_j)}{|\mathbf{r}_i-\mathbf{r}_j|^2}\right]\left[\mathbf{I}_3 - \frac{1}{2}\hat{\mathbf{t}}_j^T\hat{\mathbf{t}}_j\right]\mathbf{V}_j, \tag{A.4}$$

where $\mathbf{V}_i = d\mathbf{r}_i/dt$ is the velocity of the ith vertex relative to the fluid and $\mathbf{I}_3$ is the 3D identity matrix. We note that this is an expansion in inverse powers of $\log(L/r)$ and includes the leading nonlocal hydrodynamic interactions which are important for capturing the behavior in our experiments. Finally, each vertex is assumed to have a mass $m_i = \Delta l_i \rho\pi r^2$ so that the velocity, in the unconstrained step[29], is updated in each time step Δt according to

$$\mathbf{V}_i(t+\Delta t) = \mathbf{V}_i(t) + \frac{\mathbf{F}_i^b + \mathbf{F}_i^{drag}}{m_i}\Delta t. \tag{A.5}$$

The inextensibility constraint is implemented numerically using a fast projection method after each time step[29]. In order to simulate the extrusion process, we added vertices at the extruding end (inlet point in Figs. A5 C-D) at regular time intervals. The vertices are attached elastically to the rest of the rod and provided with an extrusion velocity, and the velocities and positions of all vertices are updated according to (A.5). Implementing this simulation in C++ code, we first perform a series of checks by comparing the results of the simulation to experiments on sedimenting elastic rods in water, analytical calculations for beam buckling, gravity loading, and the known

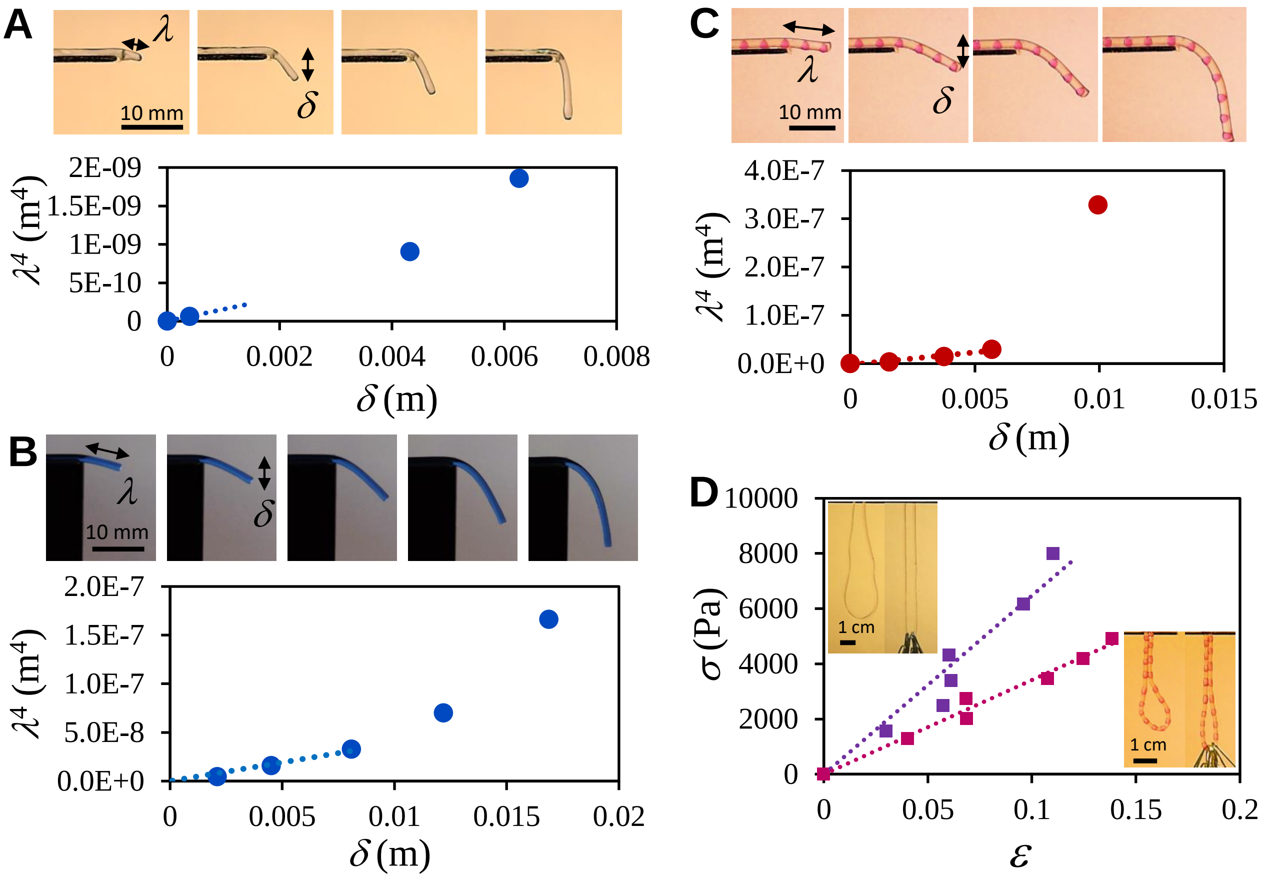

Fig. A3 Direct estimation of bending moduli B and elastic moduli E of pure alginate filaments and composite oil-embedded filaments. (A) Measurement of deflections δ of a crosslinked tube (extracted from the calcium bath seconds after it has formed) of length λ due to gravity. Plotting λ^4 as a function of δ yields a slope of $2Er^2/\rho g$ in the linear regime, which gives the elastic modulus E of the alginate tube to be 2.7 kPa. (B) Measurement of λ^4 of a crosslinked tube (extracted from the calcium bath several minutes after it has formed) as a function of δ yields an elastic modulus E of the alginate tube to be 48 kPa. (C) Measurement of deflections δ of a composite tube ($(Q_o-Q_i)/(Q_o+Q_i)$=0.7, Fig. 5C, filament 3) with silicone oil inclusions to estimate effective elastic modulus of the composite tube E_c. Plotting λ^4 as a function of δ yields the elastic modulus E_c of the alginate tube to be 36 kPa. (D) Two examples of the stress (σ)-strain (ε) curves obtained for measuring elastic moduli of the pure alginate tubes ($(Q_o-Q_i)/(Q_o+Q_i)$=1) and oil-alginate composite tubes ($(Q_o-Q_i)/(Q_o+Q_i)$=0.3), where E_{alg}=71kPa (top) and E_c=35kPa (bottom). The normalized elastic moduli (E_c/E_{alg}) for these two datasets are reported in Fig. 5D.

results for the spool-coiling of a rope falling under gravity onto the ground and get results quantitatively consistent with theory and experiments[2,30,31] (Figs. A5 B-D and Movie S4).

To deploy the simulation for a submerged jelling jet, we start with a naturally straight fully crosslinked filament and only keep the first-order (local hydrodynamic interaction) terms in $1/\log(L/r)$ in (A.3) for the viscous drag forces. By using experimentally motivated parameters values (Figs. A5 E and Movie S4) we find that although the filament starts to coil, over time the coils become disordered in space and unravel in time starting at the bottom free end. The disorder is likely due to the lack of accounting for nonlocal hydrodynamic interactions of the curved filament, while the unraveling is likely due to lack of accounting for cross linking in our experiments, where the curvature of the rod freezes (Fig. A4) and the Young's modulus of the tube material increases over time (Figs. A3 A-B), from which we extract the Young's modulus at the time of coiling by requiring that $R \approx 0.4(B/\mu v)^{1/3}$ (Fig. 2B); this yields $E = 50$ Pa.

To test these hypotheses, we included the second-order terms in $1/\log(L/r)$ and also added the effects of cross linking to the simulation by updating the natural curvature of the rods at each time step in the direction of the actual curvature with a time scale $\tau = 1s^{-1}$, corresponding to a slow freezing of the natural curvature even as the filament coils (assumed to follow a simple first-order process). We find that this suffices to capture the experimentally observed behavior associated with regular coiling seen in experiments (Fig. A5 F), and compares well with the experimental results shown in Fig. 2 and Fig. A1.

A.4 Movie Captions

Movie S1: Viscous drag induced instability of an extruded polymerizing jet of 2% sodium alginate (Q_o=2 ml/min and needle diameter $d = 0.41$mm) entering in a water bath containing 150 mM calcium chloride salt.

Movie S2: Four regimes of instability of the submerged jelling jet of 2% sodium alginate in 150mM calcium aqueous bath,

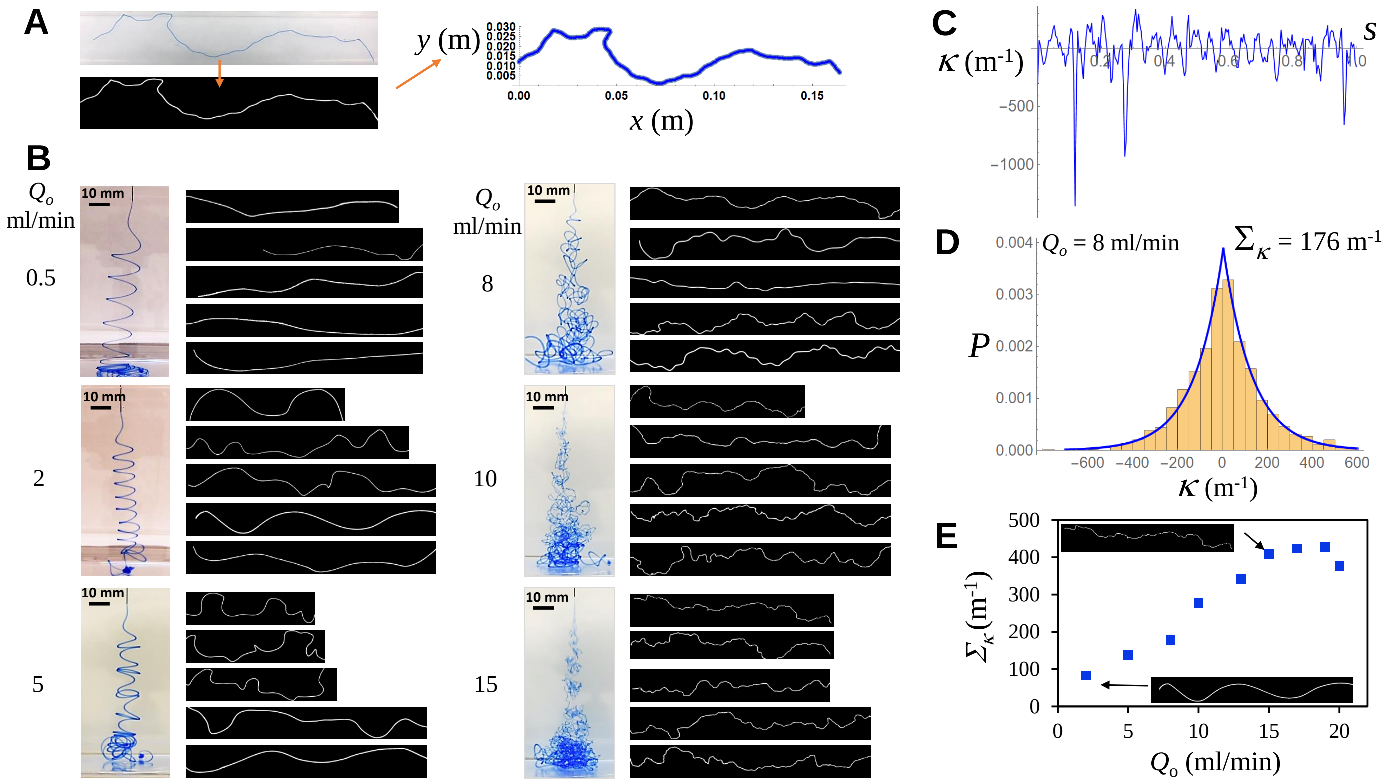

Fig. A4 Estimating the planar curvature of alginate tubes at high extrusion rates: Panel (A) shows the sequence of steps performed to obtain a smooth fit to the curves from images. First the image is binarized with pixel values corresponding to the curve of interest equal to one and zero everywhere else. Then, using a calibrated image, the (x,y) Cartesian coordinates of the curve are extracted. Finally a moving least squared approximation is used to obtain a smooth representation of the surface[26,27]. (B) For the needle size 22G ($d = 0.41$mm), varying the extrusion rate of the alginate yields smooth gently sinuous tubes at low rates ($Q_o < 8$ ml/min) to rough tubes at higher rates ($Q_o \geq 8$ ml/min), with 5 examples of the tube segments for each Q_o. (C) Curvature of the data in (A) as a function of arc length. Panel (D) shows the corresponding curvature histogram, where the curvature values comes from multiple samples for the 22G ($d = 0.41$mm) needle at $Q_o = 8$ml/min. The blue curve shows the best fitting distribution to the data. (E) Characterization of the chaotic regime via standard deviation of curvature (Σ_κ) of the gel tubes formed at high extrusion rates for a specific needle (here 22G, $d = 0.41$mm). As Q_o increases, Σ_κ increases and then saturates at very high rates due to finite thickness of the tubes.

namely: (i) gravity driven coiling (needle diameter $d = 0.84$mm, extrusion rate Q_o= 0.5 ml/min) (ii) drag induced coiling (needle diameter $d = 0.84$mm, Q_o= 5 ml/min), (iii) period doubling (needle diameter $d = 0.6$mm, Q_o= 5 ml/min) and (iv) chaotic crumpling (needle diameter $d = 0.6$mm, Q_o= 15 ml/min). Snapshots of these four regimes and the phase space are shown in Fig. 1B.

Movie S3: Four videos (1x speed) showing the chaotic crumpling of the submerged jelling jet of 2% sodium alginate in 150mM calcium aqueous bath for a fixed needle size ($d = 0.16$mm) and increasing extrusion rate Q_o=8, 10, 15, 20 ml/min. Snapshots of the chaotic crumpling and characterization of their plume angles are shown in Fig. 4.

Movie S4: Results from the 3D simulation of injected elastic threads: (A) classical gravity induced rope coiling with vanishing drag. Parameters used are: $v = 1$cm/s, $d = 1.5$mm, linear density $\rho_L = 2.9$kg m^{-1}, $E = 8.5$MPa and $\ell_g \equiv (Er^2/\rho g)^{1/3}$. The resulting radius of coiling is consistent with the experiments done in[2]. (B) Long time behavior of drag induced coiling without crosslinking and hydrodynamic interactions. The coils at the free end unwind. Parameters used: $E = 4.8$kPa, $Q = 10$ml/min, $d = 1$mm, $\Delta\rho = 15$kg/m^3 and $\mu = 0.001$Pa.s. (C) Adding crosslinking and hydrodynamic interactions, we get regular stacks of coils. After reaching a steady state, vertices are removed from the free end to speed up the simulation. Parameters used: $E = 2.7$kPa, $Q = 1$ml/min, $d = 0.8$mm, $\Delta\rho = 5$kg/m^3 and $\mu = 0.01$Pa.s.

Movie S5: Controlled patterning of co-extruded jet with outer sodium alginate (Q_o= 20ml/min) and inner red dyed silicone oil (Q_i= 10ml/min) entering an aqueous calcium bath. The size of the inclusions are selected due to pinch-off instability of the internal oil jet. The alginate-oil meet at a T-junction before entering the calcium aqueous bath through a common needle tip, where outer alginate needle (15G, d= 1.4mm) and oil needle (18G, d= 0.84mm). The resulting composite tube is buoyant and floats up at the interface of air-aqueous calcium bath.

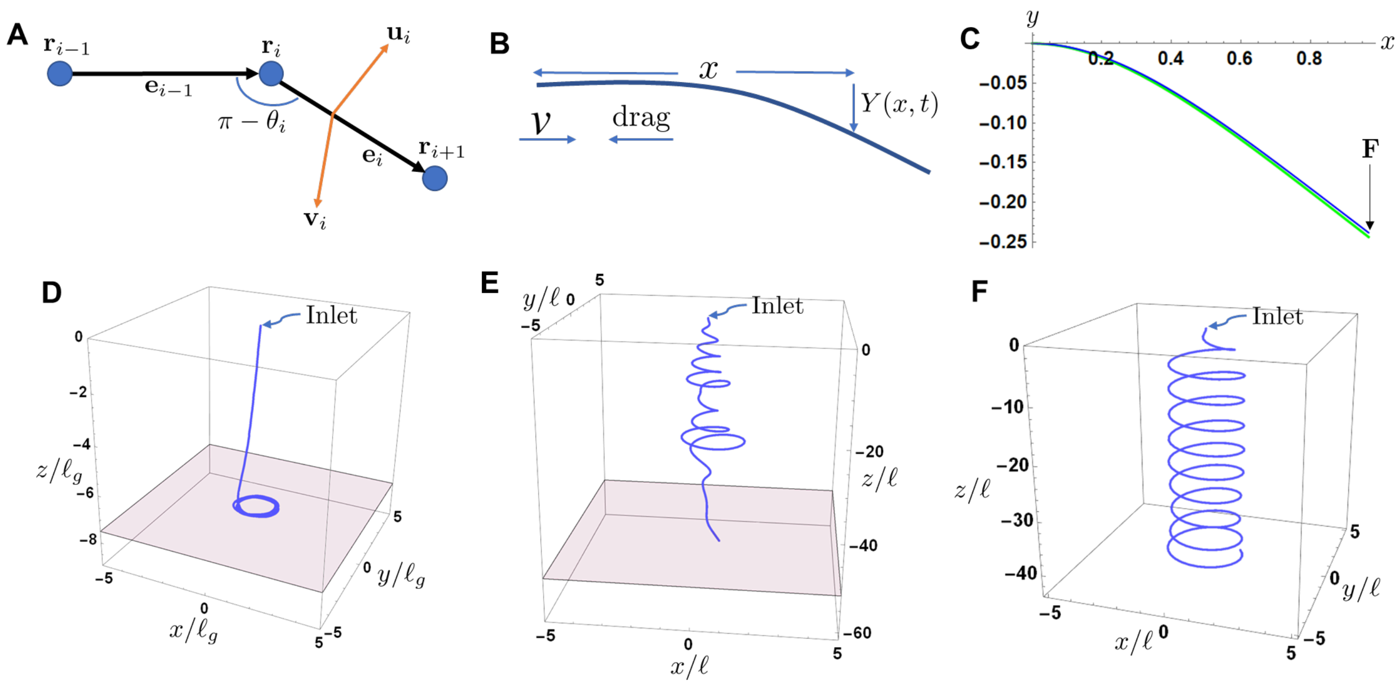

Fig. A5 Numerical simulations of drag induced coiling. (A) The discretized rods composed of vertices and edges. $\mathbf{r}_i$, $0 \leq i \leq N+1$, $\mathbf{e}_i = \mathbf{r}_{i+1} - \mathbf{r}_i$ are the edge vectors and θ_i is the angle between two edge vectors meeting at the vertex i. (B) Drag induced instability of a filament with length L and bending stiffness B, moving at a speed v in a bath μ. (C) Beam under tip loading from both simulation and theory. (D) Simulation of a rope falling under gravity onto the ground with no drag. Here $v = 1$cm/s, $d = 1.5$mm, $\rho = 1641$kg/m^3, $E = 8.5$MPa and $\ell_g \equiv (Er^2/\rho g)^{1/3}$. The resulting radius of coiling is consistent with the experiments done in Ref.[2] for a drop height of 0.5m. (E) Simulations of drag induced coiling for a naturally straight, fully crosslinked, rod. Over time the coils produced in the simulation start to unwind due to lack of forces maintaining the curvature. Parameters used: $E = 4.8$kPa, $Q = 10$ml/min, $d = 1$mm, $\Delta\rho = 15$kg/m^3. (F) Adding the leading nonlocal hydrodynamic interaction terms (see text) and the effects of slow change in the natural curvature of the filament (see text) in the simulation, we get the regular coiling observed in the experiments (see movie S4). The parameters used are $E = 2.7$kPa, $Q = 1$ml/min, $d = 0.8$mm, $\Delta\rho = 5$kg/m^3 and $\mu = 0.01$ Pa.s.